Karbon, M., Soja, B., Nilsson, T., Deng, Z., Heinkelmann, R., Schuh, H. (2017): Earth orientation parameters from VLBI determined with a Kalman filter. - *Geodesy and Geodynamics*, *8*, 6, pp. 396—407.

DOI: http://doi.org/10.1016/j.geog.2017.05.006

Geodesy and Geodynamics 8 (2017) 396–407

Contents lists available at ScienceDirect

Geodesy and Geodynamics

journal homepages: www.keaipublishing.com/en/journals/geog;
http://www.jgg09.com/jweb_ddcl_en/EN/volumn/home.shtml

Earth orientation parameters from VLBI determined with a Kalman filter

Maria Karbon [a, *], Benedikt Soja [b], Tobias Nilsson [a], Zhiguo Deng [a], Robert Heinkelmann [a], Harald Schuh [a, c]

[a] GFZ German Research Centre for Geosciences, Telegrafenberg A17, Potsdam, Germany
[b] Jet Propulsion Laboratory, California Institute of Technology, Pasadena, CA, USA
[c] Technical University of Berlin, Straβe des 17. Juni 135, Berlin, Germany

ARTICLE INFO

Article history:
Received 24 November 2016
Received in revised form
23 May 2017
Accepted 24 May 2017
Available online 6 September 2017

Keywords:
VLBI
Earth rotation
CONT14
Kalman filter
Data analysis
Least squares
GPS

ABSTRACT

This paper introduces the reader to our Kalman filter developed for geodetic VLBI (very long baseline interferometry) data analysis. The focus lies on the EOP (Earth Orientation Parameter) determination based on the Continuous VLBI Campaign 2014 (CONT14) data, but also earlier CONT campaigns are analyzed. For validation and comparison purposes we use EOP determined with the classical LSM (least squares method) estimated from the same VLBI data set as the Kalman solution with a daily resolution. To gain higher resolved EOP from LSM we run solutions which yield hourly estimates for polar motion and dUT1 = Universal Time (UT1) − Coordinated Universal Time (UTC). As an external validation data set we use a GPS (Global Positioning System) solution providing hourly polar motion results.

Further, we describe our approach for determining the noise driving the Kalman filter. It has to be chosen carefully, since it can lead to a significant degradation of the results. We illustrate this issue in context with the de-correlation of polar motion and nutation.

Finally, we find that the agreement with respect to GPS can be improved by up to 50% using our filter compared to the LSM approach, reaching a similar precision than the GPS solution. Especially the power of erroneous high-frequency signals can be reduced dramatically, opening up new possibilities for high-frequency EOP studies and investigations of the models involved in VLBI data analysis.

We prove that the Kalman filter is more than on par with the classical least squares method and that it is a valuable alternative, especially on the advent of the VLBI2010 Global Observing System and within the GGOS frame work.

1. Introduction

Geodetic VLBI (very long baseline interferometry) is one of the primary space geodetic techniques [1,2]. It substantially contributes to the International Terrestrial Reference Frame [3] and is the only technique able to realize the ICRF (International Celestial Reference Frame) [4]. It can provide the full set of EOP (Earth Orientation Parameters) which are needed for the transformation between the terrestrial and the celestial frames. The five EOP are polar motion (x-pole and y-pole), universal time (UT1), and celestial pole offsets (dX and dY). VLBI is unique for long-term observation of UT1 and precession/nutation, as satellite-based techniques (e.g. global navigation satellite systems, GNSS) suffer from the correlation between these parameters and the ascending nodes of the satellite orbits. Nonetheless, polar motion estimates from GNSS usually have less scatter than results of VLBI or SLR (Satellite Laser Ranging) due to the larger number of stations that provide continuous observations to several satellites at once

* Corresponding author.
E-mail address: karbon@gfz-potsdam.de (M. Karbon).

Peer review under responsibility of Institute of Seismology, China Earthquake Administration.

Production and Hosting by Elsevier on behalf of KeAi

http://dx.doi.org/10.1016/j.geog.2017.05.006

within the rather homogeneous distributed global IGS (International GNSS Service) [5] network.

Due to monetary, technological, and personnel restrictions the current VLBI network is not able to observe continuously. Coordinated by the International VLBI Service, IVS [1], usually only two to four 24 h sessions are observed per week, comprising five to ten stations. Two sessions per week, so called rapid-turn-around sessions, are primarily aimed at the estimation of EOP: the IVS-R1 session on Mondays/Tuesdays and the IVS-R4 session on Thursdays/Fridays. The limited observing time of 24 h, small network size and the discontinuities between the sessions greatly restrict the possibility to investigate sub-daily phenomena. Hence, since the mid-nineties special VLBI campaigns have been performed to demonstrate the capabilities of the current geodetic VLBI system: the so called CONT campaigns, where continuous observations for up to two weeks are conducted. The data from these campaigns have been used in numerous studies, e.g. investigations of tropospheric delays [6], ionospheric studies [7] or time transfer applications [8].

Several authors looked at the EOP estimated from CONT campaigns, focusing on sub-daily variations, e.g. Refs. [9–12]. These sessions allow a comparison and evaluation of the models involved in the analysis, as well as a detection of artifacts or irregular non-periodic variations. Especially CONT02 revealed irregular EOP variations including a significant retrograde signal with a period of −8 h, e.g. Refs. [10,11]. However, this signal could not be found in the following CONT campaigns, e.g. Refs. [9,10,13,14]. All the authors found harmonic signals at the diurnal and semi-diurnal frequencies, but a ter-diurnal signal was not detected. Nilsson et al. [12] connected this period at −8 h to errors in the CRF coordinates. However, the reason for most of the unexplained signals seen in the EOP spectra from the CONT campaigns may be due to deficiencies in the IERS (International Earth Rotation and Reference System Service) [15] Conventions (2010) model for high-frequency EOP variations.

Despite the large number of investigations done on EOP in connection with CONT campaigns, no final overall conclusion could be drawn about the EOP variations determined by VLBI. Thus, leaving a vital and ample research field.

In this work we investigate the accuracy of the EOP determined with our KAL (Kalman filter) designed in anticipation of the future VGOS (VLBI2010 Global Observing System) [16]. We analyze the data from the CONT campaigns observed since 2002, focusing on the latest, namely CONT14, observed in May 2014. We assess the quality and the performance of KAL as a post processing tool, by comparing it to the solution provided by the classical least squares method (LSM). For an external validation we use a GPS solution determined from TIGA (Tide Gauge Benchmark Monitoring) GPS reprocessing [17]. Section 2 gives an introduction into the CONT campaigns since 2002. In Sect. 3 the data analysis is described for all approaches, for VLBI the LSM (least squares method) and the KAL (Kalman filter) are discussed, for GPS the strategy applied within the TIGA project. Here also our approach used for the determination of the noise levels driving our filter is introduced. Section 4 is dedicated to the results. We look at the performance of LSM and KAL and compare the estimated EOP to the ones derived by GPS. Here we also demonstrate the impact of the chosen noise model for the Kalman filter. Section 5 completes the paper with conclusions, possible developments and outlook for further applications for our filter.

2. The CONT campaigns

The purpose of the CONT campaigns is to acquire state-of-the-art VLBI data over a time period of about two weeks to demonstrate the highest accuracy of which the current VLBI system is capable. During the history of the CONT campaigns the network of involved stations is continuously growing, and technical aspects, such as the recording data rate, have been constantly improved. The first CONT campaigns were performed in 1994 and 1995, and since 2002 about every 3 years one CONT campaign was scheduled. Table 1 gives some basic information like observation period, number of stations and network volume of the CONT campaigns included in this study, i.e. 2002–2014, as the previous ones do not permit the estimation of sub-daily EOP at the desired accuracy level.

Although CONT sessions are called continuous, they are not in the strict sense of the word. To ensure the functionality of the telescope, system checks are performed at each station. During that time the telescope is not observing, thus leaving a gap in the observations. For CONT02 and CONT05 these checks were performed at each station within the last 30 min of the session, hence the campaign is not completely continuous. Starting with CONT08 the maintenance slots were set at different epochs for different stations to avoid periods without observations. Further, due to technical restrictions, the data is not recorded as one data set, but separated into smaller sessions, each containing the observations of approximately 24 h. The individual sessions are then correlated separately, in case of CONT02 and CONT05 at several different centers, whereas the following CONT campaigns were all correlated at one center to assure the same setup in the correlation and fringe processes.

CONT14 is the most recent campaign of continuous VLBI sessions, observed in May 2014, from the 6th at 00:00 UTC through the 20th at 23:59 UTC. Fig. 1 shows the geographic distribution of the 17 participating stations, and Table 2 gives the positions as well as the average number of observations per day. All data were

Table 1
Observation period, number of stations, number of scans, network volume and data recording rate for the CONT since 2002. The numbers in brackets show the number of stations out of the total which are situated on the southern hemisphere, and the average number of scans per station.

CONT	Obs. period UTC	# Stat. (south)	# Scans (per stat.)	Volume (Mm^3)	Mb/s
02	16.10. 18:00 31.10. 17:45	8 (1)	6900 (870)	92	128
05	12.09. 17:00 27.09. 16:30	11 (2)	12,900 (1170)	265	256
08	12.08. 00:00 26.08. 23:59	11 (2)	17,300 (1570)	269	512
11	15.09. 00:00 29.09. 23:59	15 (5)	16,400 (1100)	485	512
14	06.05. 00:00 20.05. 23:59	17 (6)	23,100 (1360)	465	512

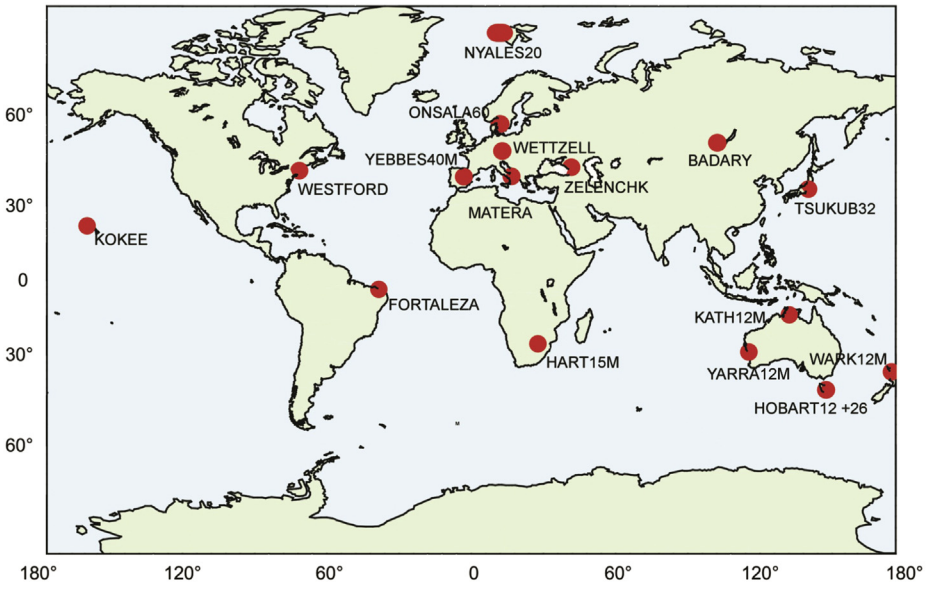

Fig. 1. The CONT14 station network.

Table 2
Stations participating in the CONT14 campaign.

Station	Lat. (°)	Lon. (°)	h (m)	# Obs./day
Badary	51.77	102.23	822	2274
Fortaleza	−3.88	−38.48	23	1254
HartRAO	−25.98	27.69	1416	1457
Hobart 26 m	−42.81	147.44	65	1225
Hobart 12 m	−42.81	147.44	41	1279
Katherine 12 m	−14.38	132.15	189	1587
Kokee Park	22.13	159.67	1177	1881
Matera	40.65	16.70	543	2270
Ny-Alesund	78.93	11.84	87	2684
Onsala 20 m	57.40	11.93	59	2573
Tsukuba 32 m	36.10	140.09	85	2446
Warkworth	−36.84	174.66	128	1203
Westford	42.61	−71.49	87	2342
Wettzell	49.15	12.88	669	2702
Yarragadee	−29.05	115.35	248	1426
Yebes 40 m	40.52	−3.09	989	2429
Zelenchukskaya	43.79	41.57	1175	2148

correlated at a single DiFX software correlator located at the Max Planck Institute for Radio Astronomy in Bonn [18]. The large network of CONT14 with its relatively good global geographical distribution between northern and southern hemispheres features a large volume, as geodetic VLBI often suffers from an imbalance in the distribution. Malkin [19] demonstrated that the network volume is correlated with the precision of the VLBI EOP determination. Thus, more accurate and precise EOP can be expected from CONT14 compared to the ones from the early 2000s or from standard IVS-R1 and IVS-R4 with an average of 9.5 participating stations. The errors depending on the recording rate follow a power law, hence, increasing the bit rate while keeping the same integration time, the error of observations can be expected to be lower.

3. Data analysis

The data of the CONT14 campaign were downloaded from the IVS website (http://ivscc.gsfc.nasa.gov) in NGS-format [20]. The group delay ambiguities of these observations were already solved and the ionospheric delays calculated. All the stations delivered suitable data for all days, although some stations showed gaps in the data acquisition, for example on May 11th Matera delivered no data after the first 8 h due to problems with the Mark5B recorder, and Wettzell missed about 3.5 h because of servo failure. Due to the stable network and dense observations the effect of such gaps is negligible for the study presented here.

The same procedure concerning data acquisition and processing was followed for all CONT campaigns included in this study. No campaign-specific constraining, station specific parametrization or tuning in any form was performed. All the models, frames and parametrizations involved in the analysis for all techniques are summarized in Table 3.

3.1. LSM (Least squares method)

For the standard LSM solution the VLBI data were analyzed with the GFZ version of the Vienna VLBI Software [21,22], VieVS@GFZ. The models used in the analysis follow the IERS Conventions 2010 [15]. For the modeling of the tropospheric delays we used the Vienna mapping functions VMF1 [23], and we estimated the zenith wet delays and the tropospheric gradients as continuous piece-wise linear functions with 1 h and 6 h interval lengths, respectively. The station clocks were modeled as pice-wise linear functions; a second-order polynomial for each day, superimposed with continuous piece-wise linear offsets every hour. The datum of the station coordinates was realized by applying no-net-translation (NNT) and no-net-rotation (NNR) conditions w.r.t. the coordinates of the VTRF2008 catalog [24]. The stations not contained in VTRF2008, for example for CONT14 Warkworth, Hobart 12, HartRAO, Yebes, Yarragadee, Katherine, and Tsukuba as it was affected by an earthquake, were excluded from the NNR and NNT constraints. The radio source coordinates of the defining sources were fixed to their ICRF2 positions [4], the special handling sources were session-wise reduced.

Firstly, each of the 15 one-day long CONT sessions were analyzed individually, forming a solution with one full set of EOP for each 24 h session. For the second solution an interval length of 1 h for the continuous piece-wise linear functions for the EOP was

Table 3
Parametrization, models, and frames of the various solutions.

Parameters, models & frames	KAL	LSM interval (constraint)	GPS
	PSD		
Station coordinates	0.1 cm^2/d	1 d	1 d
Source coordinates	fixed to ICRF2	fixed to ICRF2	–
X-pole	0.12	1 h (100 mas)	1 h
Y-pole	0.13	1 h (100 mas)	1 h
UT1	4.08×10^{-4} mas^2/d	1 h (100 mas)	LOD @1 h
Celestial pole offset	0.01 mas^2/d	fixed to apriori	–
Clock parameters	23 cm^2/d	1 h (1.3 cm)	Epoch wise for sat. & receiver
ZWD_{VLBI}/ZTD_{GPS}	20 cm^2/d	1 h (1.5 cm)	1 h
Gradients	0.02 cm^2/d	6 h (0.05 cm)	24 h
Ocean tide loading	FES2004		FES2004
Atm. pressure tide loading	IERS2010		IERS2010
TRF	IVS realization of ITRF2008		IGS realization of ITRF2008
ERP	IERS 08 C04		IERS Bulletin A
Celestial pole offset (CPO)	IAU 2006/2000A		IAU 2000A

chosen. In this case the celestial pole offsets could not be estimated, due to the high correlation with retrograde polar motion and thus, they were fixed to their a priori values. To mitigate the effect of the breaks at the session borders, and to facilitate correlations between the parameters of the subsequent sessions, the obtained normal equations were stacked and solved within a global solution. This procedure allows the estimation of EOP and station positions for the entire CONT campaign, as these parameters can be de-correlated sufficiently, resulting in a continuous solution with a time resolution of 1 h for the EOP. We followed an approach similar to [13,14,25]; stacking station coordinates, EOP, zenith wet delays, and gradients.

3.2. KAL (Kalman filter)

The KAL solution generated for this study was optimized for post-processing, in other words a backwards filter and a smoother are implemented additionally to the forward filter. Here just a small introduction shall be given, a more detailed report about the application of our Kalman filter has been presented in Ref. [22].

The Kalman filter follows the sequence of observations using the state at the epoch $t-1$ to predict the state at the next epoch t. Then the predicted value is combined with the new observation to get an optimal estimation at epoch t [26]. $\boldsymbol{x}_t$ is the state vector containing the unknown parameters at epoch t. It can be recursively related to the estimates at the previous epoch $\boldsymbol{x}_{t-1}$ through

$$\boldsymbol{x}_t = \boldsymbol{F}_t \boldsymbol{x}_{t-1} + \boldsymbol{w}_t \tag{1}$$

where $\boldsymbol{F}_t \boldsymbol{x}_{t-1}$ is the prediction of $\boldsymbol{x}_t$ based on $\boldsymbol{x}_{t-1}$ and $\boldsymbol{w}_t$ is the assumed error in the prediction. $\boldsymbol{F}$ is the state transition matrix. The covariance matrix of the total errors $\boldsymbol{P}_t^-$ can be calculated by

$$\boldsymbol{P}_t^- = \boldsymbol{F}_t \boldsymbol{P}_{t-1} \boldsymbol{F}_t^{\mathrm{T}} + \boldsymbol{Q}_t \tag{2}$$

with $\boldsymbol{P}_{t-1}$ denoting the variance-covariance matrix of $\boldsymbol{x}_{t-1}$ and $\boldsymbol{Q}_t$ the variance-covariance matrix of the prediction error $\boldsymbol{w}_t$. The observations $\boldsymbol{z}_t$ at epoch t are

$$\boldsymbol{z}_t = \boldsymbol{H}_t \boldsymbol{x}_t + \boldsymbol{v}_t \tag{3}$$

$\boldsymbol{H}_t$ is the observation matrix and $\boldsymbol{v}_t$ is the observation noise. The observation matrix $\boldsymbol{H}$ consists of the partial derivatives of the delay with respect to the parameters. To get the optimal estimation for $\boldsymbol{x}_t$ and its covariance matrix $\boldsymbol{P}_t$ the prediction $\boldsymbol{x}_t^-$ and the observation $\boldsymbol{z}_t$ can be combined using

$$\begin{aligned} \boldsymbol{x}_t &= \boldsymbol{x}_t^- + \boldsymbol{K}_t \left(\boldsymbol{z}_t - \boldsymbol{H} x_t^- \right) \\ \boldsymbol{P}_t &= (\boldsymbol{I} - \boldsymbol{K}_t \boldsymbol{H}_t) \boldsymbol{P}_t^- \end{aligned} \tag{4}$$

with the Kalman gain $\boldsymbol{K}_t$

$$\boldsymbol{K}_t = \boldsymbol{P}_t^- \boldsymbol{H}_t^{\mathrm{T}} \left(\boldsymbol{H}_t \boldsymbol{P}_t^- \boldsymbol{H}_t^{\mathrm{T}} + \boldsymbol{R}_t \right)^{-1} \tag{5}$$

where $\boldsymbol{R}_t$ is the covariance matrix of the observation noise $\boldsymbol{v}_t$.

In our filter the state transition matrix $\boldsymbol{F}$ is realized as a matrix with dimension $[n \times n]$ with n being the number of parameters. The clock parameters are the only ones having a non-zero off-diagonal element describing the relationship between constant and linear clock parameters. Since all deterministic models have already been applied within VieVS@GFZ, only the stochastic processes remain to be modeled at this stage. All parameters are modeled as a random walk process, except the clock offsets, which are modeled as an integrated random walk (e.g. Ref. [27]). The noise parameters for the process noise covariance matrix $\boldsymbol{Q}$ are determined using the Allan standard deviation [28]. More details on the EOP noise level determination are given in Sect. 3.2.1. For the clocks, these noise parameters were determined empirically. Soja et al. [29] gave a comprehensive insight into the noise determination for the tropospheric parameters, as well as for the stations.

For the post-processing, a backward filter and a smoother are implemented additionally, as the combination of a forward and a backward recursion is considered to have utilized all available information and thus, can be expected to perform better than a forward filter only [27]. For the backward filter the whole process introduced above is inverted. Starting point becomes the optimal estimation $\boldsymbol{x}_{t+n}$ of the forward filter at the final epoch $t + n$ with the variance-covariance matrix $\boldsymbol{P}_{t+n}$. Then the filter is run again with the time increment -1.

Finally, within the smoothing the two filter runs (forward and backward) are combined in an optimal way, where the index f denotes the forward and b the backward filtered parameters:

$$\begin{aligned} \boldsymbol{P}_t &= \left(\boldsymbol{P}_{tf}^{-1} + \boldsymbol{P}_{tb}^{-1} \right)^{-1} \\ \boldsymbol{x}_t &= \boldsymbol{P}_t \left(\boldsymbol{P}_{tf}^{-1} \boldsymbol{x}_t f + \boldsymbol{P}_{tb}^{-1} \boldsymbol{x}_{tb} \right) \end{aligned} \tag{6}$$

The transition from one session to the next (since CONT08 at 00 UTC) is made continuous by setting the a priori $\boldsymbol{x}_0$ equal to the final best estimate $\boldsymbol{x}$ of the previous session, except for the clocks.

3.2.1. Noise modeling

The noise driving the parameters is the most sensitive part in the Kalman filter, as it describes within the stochastic model the evolution of the parameters through time. The covariance matrix of the observation noise $\boldsymbol{Q}_t$ is defined as:

$$\boldsymbol{Q}_t \equiv \left\langle w_t w_t^{\mathrm{T}} \right\rangle \tag{7}$$

For short temporal distances between the observations (<1000 s), $\boldsymbol{Q}_t$ can be considered equal to $\Phi\Delta t$, where Φ denotes the power spectral density (PSD) of the white noise process w. PSD is the preferred measure to characterize signals in the frequency domain as it allows the characterization of noise through power-laws, e.g. white noise follows the power law of $1/f^0$, flicker noise of $1/f^\alpha$ with $0 < \alpha < 2$, random walk of $1/f^2$, and integrated random walk of $1/f^4$. To identify the type of the stochastic process driving the EOP and consequently to determine the PSD from it, we use its counterpart in the time-domain, the Allan standard deviation (ASD, [28]):

$$\boldsymbol{\sigma}_x^2(\tau) = (p_{t+\tau} - p_t)^2 \Big/ \tau^2, \tag{8}$$

with $p(t)$ being the value of the process at the time t and τ denoting the sampling time. Plotting $\boldsymbol{\sigma}_x^2(\tau)$ on logarithmically scaled axes allows the identification of the noise characteristics by the slopes in the time-domain.

Fig. 2 shows the Allan Standard Deviation for GPS in red, for LSM in green and KAL in blue, starting for 1 h to up one day. For this KAL solution the PSD values were taken from Ref. [30]; and the Allan Standard Deviation was then calculated from that preliminary solution. The interval was chosen as 1 h. The black lines show power lines: the solid line the ASD for flicker noise with $k = -0.75$, the dashed line a random walk with a slope of $k = -1/2$, and the dash-dotted line an integrated random walk with $k = -1/4$. We found that the flicker noise best matches the ASD of our data, as for all CONT campaigns in this study k varies between 0.7 and 0.8. Our findings agree with [31]; who found that for periods less than 40 days, flicker noise fits best. Also more recent studies conducted by Ref. [32] about EOP determination by GNSS show that polar motion has the characteristics of flicker noise.

A flicker noise process is characterized by an infinitely long memory plus short-term fluctuations. As it represents a non-linear system, the classical Kalman filter would not be the optimal choice. However, in practice flicker noise often is approximated by a random walk or by a first-order Gauss-Markov process [30,33]. Nevertheless, the estimates can be too optimistic, particularly when no measurement update is available for a long period, as the long memory of flicker noise is omitted [34].

However, as in case of CONT14 in average one observation per minute is available, and with VGOS in sight the number of observations per time will only increase, the approximation of the flicker noise through a random walk seems reasonable. Thus, for the current implementation of our Kalman filter we decided to model the EOP as a random walk process. The results presented in the next chapter prove that the filter can recover the values of EOP accurately.

To derive the PSD needed for the covariance matrix $\boldsymbol{Q}_t$ from the ASD, we make use of the following relationship, which is valid in case of a random walk:

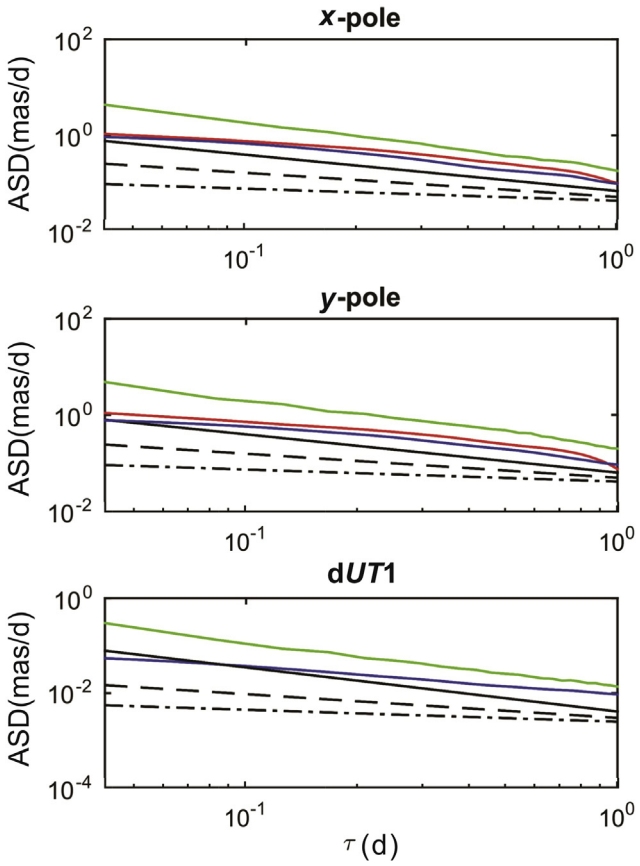

Fig. 2. Log–log plot for the ASD for GPS (red), LSM (green), and KAL (blue) for CONT14. The power lines are in black, solid line for flicker noise with $k = 0.75$, dashed line for random walk, and dash-dotted line for integrated random walk.

$$\Phi = \boldsymbol{\sigma}_x^2(\tau)\tau. \tag{9}$$

Due to the huge number of observations provided by GPS the derived EOP can be considered more accurate, than EOP derived from VLBI (law of large numbers). Additionally, the IGS network has in comparison to the VLBI network an excellent global coverage, thus the pole coordinates can be retrieved more reliably. In contrast LSM is limited by the parametrization of the estimates as continuous piecewise-linear functions, and the geometric stability of the solutions, thus the minimum interval length of the EOP estimates is 1 h. Further, compared to one set of EOP per 24 h session the formal errors deteriorate, especially at the session boundaries. Also our PSD values derived from GPS agree well with the ones from literature, whereas the ones from LSM are a factor of 10 larger.

Taking all this into account, we decided to use the mean over all CONT of the GPS noise for driving the polar motion in the Kalman filter. For dUT1 we used the ratio between the GPS and LSM values for polar motion to calculate a men conversion factor. This we used to convert the LSM noise level for dUT1 to GPS (4.081×10^{-4} ms^2/d). The noise level of nutation was determined empirically, by running several solutions with different noise levels. The one delivering the smallest residuals w.r.t. the a-priori was chosen. In Table 4 we summarize the PSD of the GPS, LSM, and KAL solutions for polar motion and dUT1, the values finally used in the KAL solution are given in bolt numbers.

Table 4
PSD of the GPS, LSM, and KAL solution for polar motion and dUT1 for all CONT, in (mas^2/d) and (ms^2/d) respectively. The mean values of GPS (bold) are used in the Kalman filter, in case of dUT1 the proportional value of LSM is used (*).

		X-pole	*Y*-pole	dUT1
CONT02	GPS	0.09	0.08	–
	LSM	3.36	1.63	0.0057
	KAL	0.03	0.02	7.9×10^{-5}
CONT05	GPS	0.16	0.20	–
	LSM	1.12	1.46	0.0049
	KAL	0.02	0.02	1.12×10^{-4}
CONT08	GPS	0.10	0.13	–
	LSM	1.44	1.38	0.0050
	KAL	0.03	0.02	1.66×10^{-4}
CONT11	GPS	0.13	0.13	–
	LSM	1.27	1.47	0.0063
	KAL	0.03	0.02	1.50×10^{-4}
CONT14	GPS	0.11	0.12	–
	LSM	0.95	1.19	0.0033
	KAL	0.04	0.03	1.14×10^{-4}
Mean	GPS	**0.12**	**0.13**	**4.08** $\times 10^{-4}$ (*)
	LSM	1.63	1.42	0.0050
	KAL	0.03	0.021	1.24×10^{-4}

3.3. TIGA GPS data processing

For our study we made use of the data provided within the International GNSS Service (IGS) Tide Gauge Benchmark Monitoring-Working Group (TIGA-WG). Within this project GNSS data from around 800 stations at or near tide gauges are analyzed, preferably on a continuous basis to provide information specifically for the vertical rates [35]. As one of the TIGA Analysis Centers the German Research Centre for Geosciences (GFZ) is contributing to the IGS TIGA Reprocessing Campaign (REPRO2, [17]). After the first reprocessing finished in 2010 some improvements were implemented into the latest GFZ software version EPOS.P8.

The TIGA data reprocessing is done in two steps, first precise satellite clocks, orbits and 1-day normal equations are generated from the IGS REPRO2 using the IGS stations. In the second step the TIGA stations, which are not already included in IGS REPRO2 are processed. Precise station coordinates are estimated in PPP mode for a single station by using the GFZ IGS reprocessing orbit and clock SP3 products. Through this the computational burden of the data processing in the network mode can be avoided, as a large number of stations can be processed in parallel. To get the final TIGA solution all normal equations of the sub-networks are stacked.

The ERP (Earth Rotation Parameters) are generally estimated with a temporal resolution of 24 h. To compare the temporally high-resolved ERP from VLBI with the TIGA GPS ones a reprocessing has been done for the time periods in question. The only difference of the new solution is: the temporal resolution of the ERP was increased to 1 h.

The models and a priories used in each technique are summarized in Table 3. The relevant differences within the processing of VLBI and GPS are the EOP, as VLBI following the IERS Conventions (2010) with IERS 08 C04 and IAU 2006/2000A is free of free core nutation (FCN), where GPS together with IERS Bulletin A and IAU 2000A, as demanded by the IGS reprocessing, does not consider the FCN. This entails different a priori values for the CPO, thus leading to a slightly different celestial pole for both techniques. Also VLBI adjusts the a priories while GNSS analysis fixes on them. Although, the impact on the ERP should be negligible for our purposes and limited to the retrograde diurnal frequency band [36]. Also the impact of the different TRF, i.e. VTRF08 and IGb08, can be considered negligible, as both are aligned with ITRF2008. ITRF2008, VTRF08 and IGb08, an updated version of IGS08, are equivalent at the global level, in the sense that they share the same underlying origin, and orientation, in case of IGb08 also scale [24,37].

4. Results

4.1. Time series

Due to the nature of GPS observations (high correlation of UT1 and the orbital elements of the satellite), only direct comparisons with polar motion can be done. For that purpose the Kalman solution was synchronized with the GPS solution, i.e. mean values of 1 h bins, ±30 min. at the integer hours, were calculated. In Fig. 3(a) the EOP estimates for CONT14 are plotted: in blue KAL, in cyan the binned KAL solution, in green the hourly LSM solution, and as black asterisks the daily LSM values, while GPS is plotted in red. At first, the offsets between the VLBI solutions and the GPS solution become evident, especially in *y*-pole (likewise in the other CONT campaigns). In Table 5 the mean values and *std* of the estimates of polar motion and dUT1 for CONT14 are listed.

The offsets of the polar motion of the VLBI solution with respect to the GPS solution may originate in the different datum definitions, as VLBI in comparison to GPS has a very sparse and inhomogeneous station distribution and thus, the impact of the network geometry needs to be considered. Also, the correlation between the EOP and the station coordinates has to be kept in mind in case of VLBI. For GPS, on the other hand, is not significant due to its large number of stations. Further, the differences in the EOP modeling, e.g. the negligence of the FCN in the GPS processing might contribute to these offsets. For *x*-pole LSM shows an offset twice as large as KAL, whereas for *y*-pole the offsets for KAL and LSM are at about the same level. When compared to the other two solutions the std of LSM is considerably larger, corresponding to the higher variation seen in the estimates. For the stacking no constraints for the estimated EOP were used, although moderately constraining the parameters or changing other models like the terrestrial datum, did not change the solution at a significant level. Also, we did not want to introduce campaign specific parametrizations for the LSM solutions.

The process noise level implemented in the Kalman filter, on the other hand, provides a smooth solution. Here the forward-backward-smoothing algorithm show its effect. For polar motion the standard deviation of the residuals w.r.t. the a-priori values of KAL is smaller than the one of GPS.

In order to take a closer look on the sub-daily EOP we subtracted daily EOP values from the individual time series, which account for most of the long period variations. These mean values were determined through the mean value of the estimates within one day, which then were interpolated linearly. For CONT14 this gives the time series shown in Fig. 3(b). As expected, also in this case the hourly LSM solution displays the largest variation ($std_{x-\mathrm{pole}} = 0.15$ *mas*, $std_{y-\mathrm{pole}} = 0.17$ mas), whereas KAL and GPS

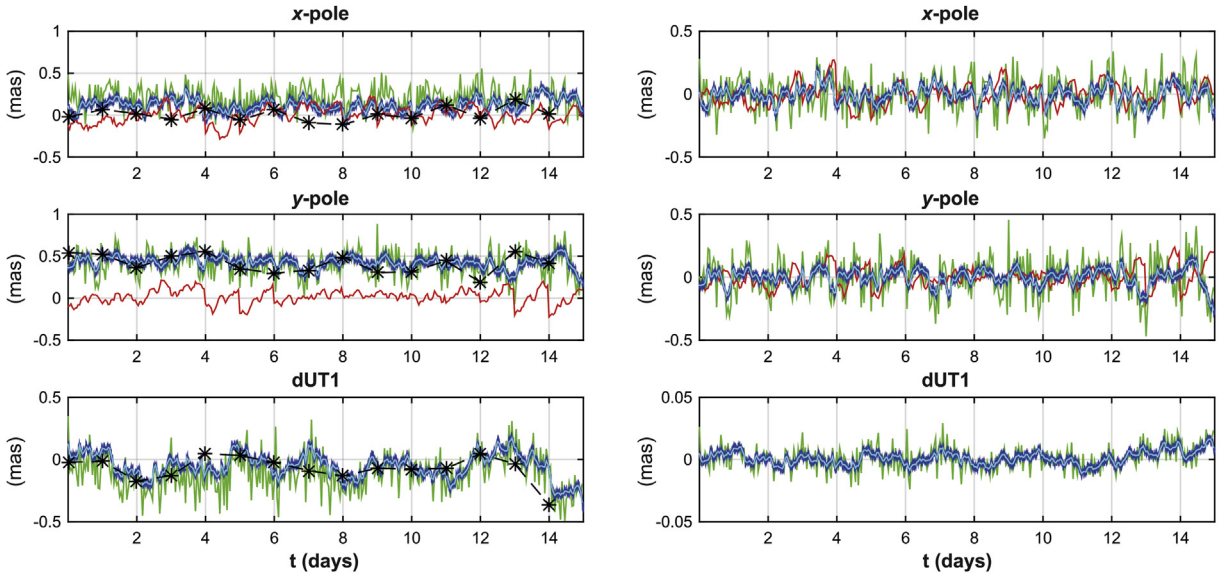

Fig. 3. a) EOP estimates for CONT14, in black the results from the daily LSM approach, in green the hourly LSM approach, in blue the Kalman estimates, in cyan the binned KAL, in red hourly polar motion estimates from GPS. **b)** EOP estimates minus daily mean values for CONT14, in black the results from the daily LSM approach, in green the hourly LSM approach, in blue the Kalman estimates, in cyan the binned KAL, in red hourly polar motion estimates from GPS.

show significantly smaller standard deviations ($std_{x-\text{pole}} \approx std_{y-\text{pole}} \approx 0.10$ mas).

4.1.1. Inter-comparison of CONT

Fig. 4 shows for all the CONT campaigns since 2002 the differences between KAL and GPS in blue, and LSM and GPS in green. Their respective daily means were removed beforehand. Each section separated by a vertical black line corresponds to a specific CONT. The red line marks the std of the LSM solution, the black line the std of the KAL solution. The numerical results are summarized in Table 6.

We can observe that with each CONT campaign the differences with respect to the GPS solution decreases, and that the KAL solutions shows on average a 40–50% smaller std compared to the LSM solution. Overall the agreement of the solutions with GPS improved by about 20% over the years, when ignoring CONT02. Our LSM solution seems to have some problems in *x*-pole as indicated by its comparable large std, an this is also visible in the spectra in Fig. 5. Also for CONT11 the *std* for *x*-pole for LSM is slightly larger than for the remaining campaigns.

A slight overall decrease in the std from CONT02 until CONT14 can be observed, as not only the station network had been growing with each CONT campaign (see Table 6), but also the recording rate has increased from 128 Mb/s for CONT02 to 256 Mb/s for CONT05 and 512 Mb/s for CONT08 and after. Since CONT08 the EOP from VLBI and from GPS have been referring to the same time interval, i.e. 0:00 to 23:59 UTC, thus, a better agreement in terms of std can be expected, as inaccuracies due to the synchronization were avoided. Also within the VLBI analysis this may improve the accuracy, as also most of the a priori values, e.g. EOP, refer to integer day epochs. Further, starting with CONT08, the maintenance gaps were scheduled for different epochs for the different stations, avoiding longer periods without observations, especially at the end of the sessions, were the system checks were done in CONT02 and CONT05. Thus, the continuity of the observation is guaranteed, avoiding weak estimates at the end of the sessions.

Table 5
Standard deviation (std) and mean values of the estimates of the VLBI solutions and the GPS solution for CONT14 for polar motion.

	X-pole (mas)		*Y*-pole (mas)		dUT1 (ms)	
	Mean	Std	Mean	Std	Mean	Std
LSM	0.207	0.136	0.404	0.153	−0.007	0.009
KAL	0.120	0.075	0.428	0.069	−0.003	0.006
GPS	0.001	0.099	0.017	0.083	–	–

4.2. Spectral analysis

To investigate the high frequency variations we calculated the Fourier spectra of the time series shown in Fig. 3(b). First, in this section, we look at them in a more general manner, then in the

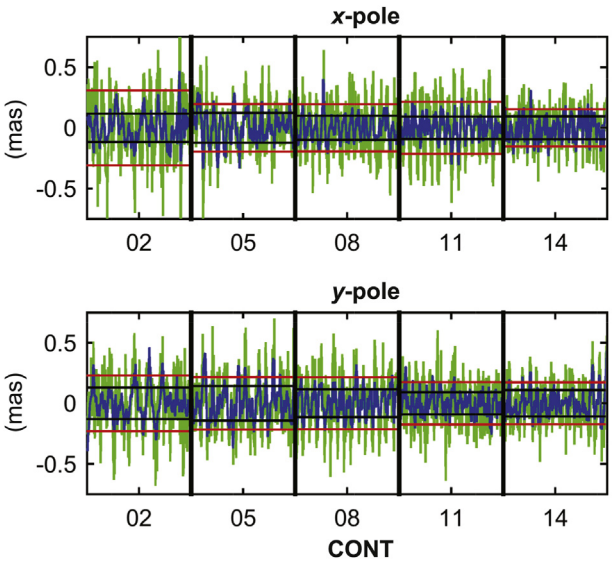

Fig. 4. Difference of the high frequency polar motion determined from KAL (blue) and LSM (green) and the GPS solution for all CONT since 2002. In red the *std* for LSM, in black for KAL. Daily values subtracted.

Table 6
Standard deviation (std) of the differences between the GPS solution and the hourly LSM and the Kalman solution after subtracting the daily mean values, for all CONT campaigns since 2002. The percentage gives the improvement of the agreement between the Kalman solution and GPS solution w.r.t. the agreement between the LSM solution and the GPS solution (unit:mas).

	X-pole			*Y*-pole		
	KAL	LSM	%	KAL	LSM	%
CONT02	0.116	0.309	62	0.129	0.229	44
CONT05	0.124	0.196	37	0.143	0.217	34
CONT08	0.098	0.194	49	0.115	0.214	47
CONT11	0.093	0.215	56	0.092	0.175	47
CONT14	0.095	0.154	38	0.109	0.173	38

following two sections in more detail covering polar motion and dUT1 separately.

The spectra for CONT14 are plotted in Fig. 6: GPS in red, LSM in green and KAL in blue. For this comparison we generated also a KAL solution where no celestial pole offsets were estimated: KAL_{woN} in cyan. The solid black line marks the 3σ confidence level calculated from LSM, the dashed black line for 1σ respectively. It should be kept in mind, that the data only cover 15 days, thus, the leakage effect might have an impact on the spectra (i.e. due to the windowing spectral components can become visible, which are not in the original signal), as well as some aliasing could occur.

LSM shows strong power at the very high frequencies, one reason is that no constraints have been applied on the EOP estimation. For GPS and KAL the spectra converge to zero for increasingly high frequencies. Looking at the spectra of the last five CONT campaigns (Fig. 5) we can observe that the overall number and amplitudes of the peaks between four and 20 h decrease from one CONT campaign to the next. Obviously the high-frequency EOP benefit greatly from the advances in the VLBI technology, for example the increased data recording rate and the larger station networks.

As expected, all solutions show significant spectral peaks in the diurnal and semi-diurnal bands, as well as several other peaks. The patterns and amplitudes of the smaller peaks of VLBI vary significantly among the five CONT campaigns. They may originate from geophysical phenomena or insufficient a priori models. For example the high-frequency EOP model as well as the ocean tide models as recommended by the IERS Conventions have shortcomings as demonstrated by several authors [9,12,21,22]. Desai

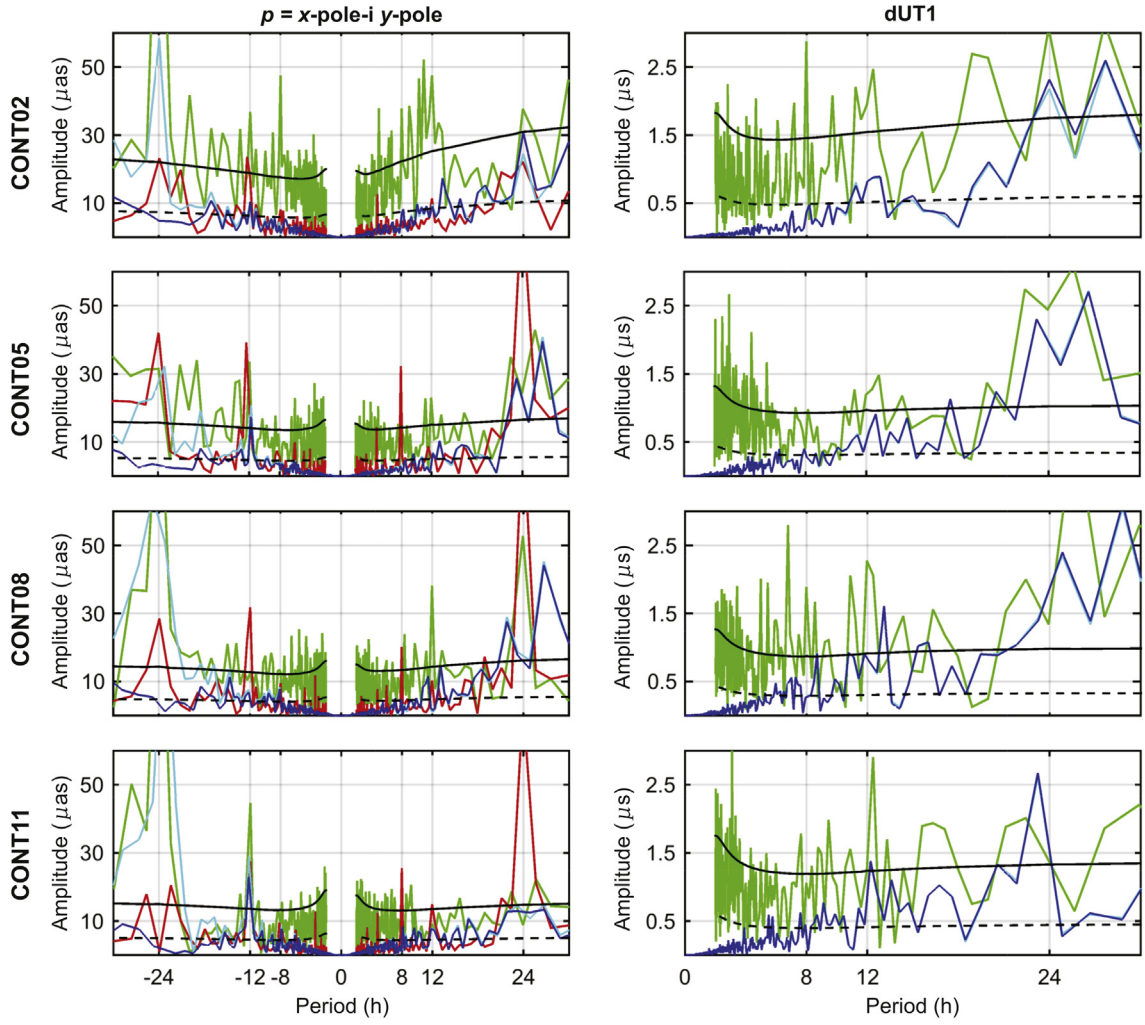

Fig. 5. Spectra ($p = x$-pole$-$i y-pole) of polar motion (left), and dUT1 (right) for the CONT since 2002. In green the hourly LSM approach, in blue the Kalman estimates, in cyan the Kalman solution without estimating the celestial pole offset, in red the polar motion estimates from GPS. In black the 3σ (solid) and 1σ (dashed) confidence level.

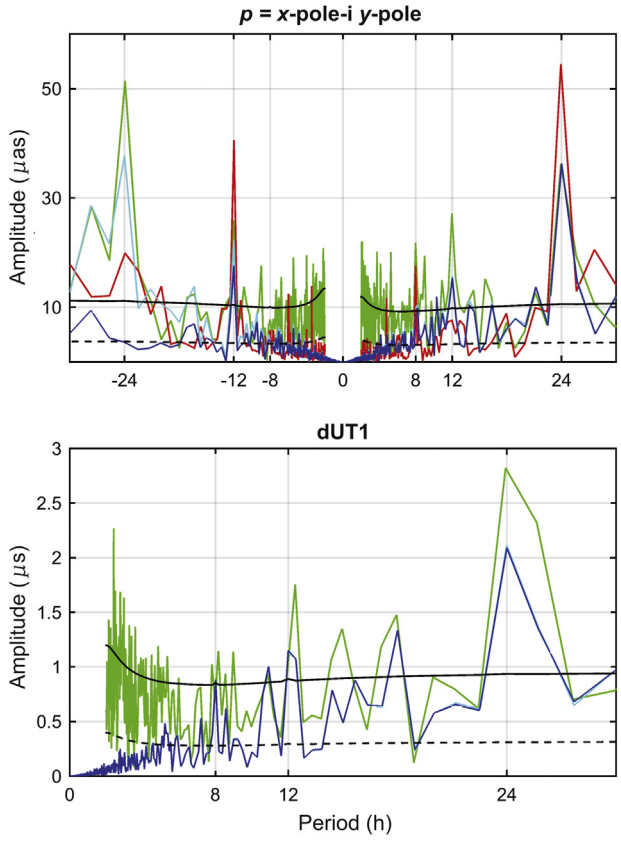

Fig. 6. Spectra ($p = x$ - pole $-$ iy - pole) of polar motion (upper plot), and dUT1 (lower plot) for CONT14. In green the hourly LSM approach, in blue the KAL, in cyan KAL without celestial pole offsets estimated, and in red the polar motion estimates from GPS. In black the 3σ (solid) and 1σ (dashed) confidence level.

and Sibois [38] showed that an updated version of the ocean tide model as recommended by the IERS, i.e. TPXO8, can significantly reduce residual polar motion at the primary frequencies, for example K1 by 16 μas. Further, this model provides improved consistencies concerning liberation. However, also deficiencies and differences in the applied processing strategies can lead to significant amplitudes. In case of GPS the peaks at ±24 + h and integer fractions of it can be explained easily, but maybe not solely, by the draconitic period of 12 sidereal hours of the GPS satellites. Steigenberger [39] supports the assumption of these peaks being artifacts of remaining systematic errors through the fact that peaks at the same periods are visible in the formal error spectra. For VLBI the peaks at 24 h can partly be attributed to the small offsets visible at the day boundaries. Such peaks at 24 h, as well as 12 h, have also been observed by other authors for other CONT campaigns, for example [9–11,13,14].

4.2.1. Polar motion

Fixing the celestial pole offsets to the a priories of IERS 08 C04 leads to a huge retrograde diurnal peak in polar motion, visible in LSM and KAL$_{woN}$. Nutation is not only driven by atmospheric and non-tidal ocean variation due to the retrograde diurnal cycle of solar heating [40,41], but also the free core nutation (FCN, [42]) is mitigated to a large extent by applying nutation corrections derived by VLBI. Additionally Brzeziński et al. [40], predicted a peak at 28.8 h retrograde with an amplitude of 31 μas due to the atmospheric normal mode ψ_1^1. This peak is clearly visible in the spectra of CONT14 of LSM and KAL$_{woN}$ with an amplitude of 26 μas, while for KAL with the estimation of the celestial pole offsets it is 20 μas smaller.

The peaks at the diurnal band can also be explained by geophysical signals. One is the tri-axiality of the Earth, however this effect is taken into account through the IERS high frequency model. Polar motion excitation through non-tidal OAM and AAM were estimated to rise to 17 μas and ~7 μas respectively [43,44], whereas [45] derived thermal driven variations in the atmospheric tides, each below 8 μas. Our findings are to some extent consistent with these results. For instance the CONT14 spectra show a distinct peak at +24 h with an amplitude of 37 μas for both KAL solutions and LSM. For CONT02 the peak is smaller for both KAL (24 μas for KAL$_{woN}$, 31 μas for KAL), whereas LSM stays at the same level. For the other campaigns both KAL spectra show two peaks, one before and one after 24 h. LSM follows that pattern, except for CONT08. These two peaks my origin in the 0.9 day and 1.2 day component of the ocean tides. Also, the limited time span of 15 days could lead to effects where several tidal components might be represented by a single peak and thus, the separation of the signals would be very difficult or impossible.

In case of the semi-diurnal band no such explanations can be given. All the studies concerning atmospheric excitation of polar motion at ±12 h report of much smaller amplitudes, e.g. Ref. [40] estimated a polar motion amplitude of 2.9 μas for the S_2 atmospheric tide and [44] of 2.6 μas.

The unexplained peak at −8 h in CONT02 detected by many authors cited in this paper, can also be seen in the LSM solution, but not as clearly in the two KAL solutions. In KAL such peaks of about 10 μas are visible also for CONT08 and CONT11. However, until now no geophysical explanations have been given for variations −8 h, although some models predict small amplitudes. For example Haas and Wünsch [10] reported about a M_3 tide with an amplitude of 0.42 μas retro- and 0.30 μas pro-grade. Nilsson et al. [12], however, explained the peak in CONT02 by an unstable source included in the ICRF2 catalog.

We performed the same test with CONT11, where we found also a peak at −8 h in the KAL solutions. Therefore, we calculated a solution where we estimated the radio source coordinates in addition to the other parameters. Nilsson et al. [12] could eliminate the peak at −8 h in CONT02 using that strategy, in our case for CONT11 the peak only slightly decreased. For KAL from 8.1 μas to 7.3 μas and for LSM from 16.5 μas to 14.8 μas. However, for CONT02 the peak in LSM is a factor of three larger than for CONT11 and for KAL there is no significant peak in CONT02 at −8 h at all.

Artz et al. [9] also detected peaks at ±6 h in the spectra of CONT02 and of CONT05, and Nilsson et al. [14] noted a lot of power in this band for CONT11. These peaks are insignificant in our results. There is no geophysical signal known causing significant variations at the quart-diurnal band.

4.2.2. dUT1

For dUT1 the most prominent peaks arise at the diurnal and semi-diurnal bands (Figs. 5 and 6). For diurnal variations thermal atmospheric and non-tidal oceanic variations can be taken into account. However, the expected amplitudes are again much smaller than the ones visible in the spectra. Brzeziński et al. [40] for example estimated amplitudes of 0.5 μas for the S_1 tide, and [10] 0.5 μas for non-tidal angular momentum. Additionally, in case of UT1 OAM and AAM tend to cancel each other out [44,46]. Keeping in mind that the periodic terms of polar motion around 8 h, 12 h and 24 h are consistent with the terms of the ocean tides, it is rather likely that the IERS high frequency model has insufficiencies.

Noticeable is the performance of both KAL solutions at periods shorter than 10 h (Figs. 5 and 6): whereas LSM is rather noisy and the amplitudes stay at a 10 μas level for polar motion and 1 μs for dUT1, KAL follows to a large extent the GPS signal and converges to zero with increasingly high frequencies. While the amount of 'real' signal at these high frequencies has to be investigated further, the level of agreement with GPS is very good.

4.3. Impact of the noise level

As mentioned in Sect. 3.2.1 we decided to use the noise level of GPS to drive our Kalman filter, not only because GPS gives more reliable results concerning ERP, but also because the noise values derived from LSM are by a factor ten bigger than the ones we found in literature. However, this inevitably leads to an conditioning of our Kalman solution towards the GPS solution. Another well known issue concerning the estimation of sub-daily EOP is, as mentioned in the sections before and illustrated in Figs. 5 and 6, the one-to-one correlation between the celestial pole offsets and a retrograde diurnal term in polar motion. In case of LSM this could be handled with applying a special constraint as shown by Refs. [47,48]. Looking at the noise level of the Kalman filter a similar concept could be applied.

For illustration we ran a KAL solution implementing the LSM noise level. The resulting spectra are shown in Fig. 7, in green the hourly LSM approach, in blue and cyan the KAL solutions with and without celestial pole offsets estimated as before. Magenta shows the KAL_{LSM} solution using the LSM noise.

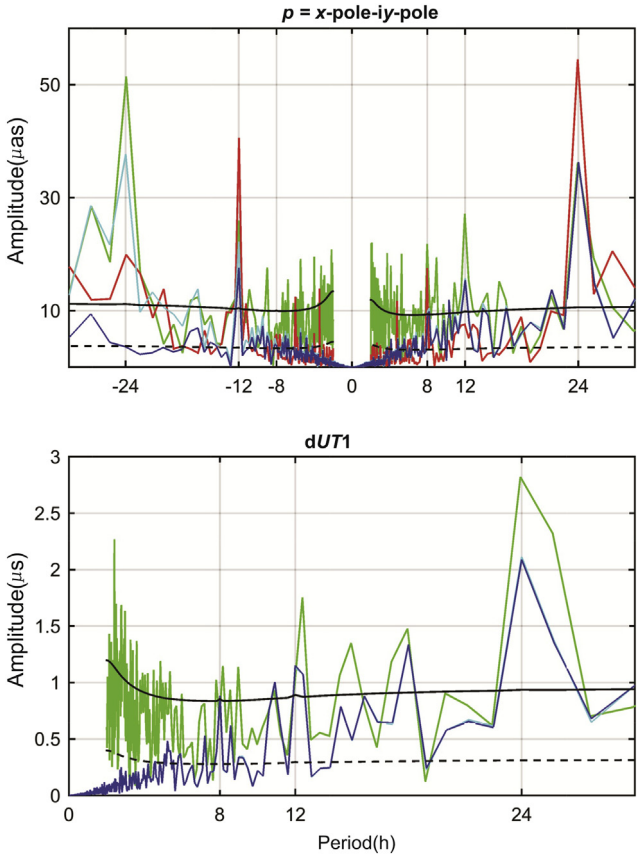

Fig. 7. Spectra ($p = x$-pole $-$ iy-pole) of polar motion (upper plot), and dUT1 (lower plot) for CONT14. In green the hourly LSM approach, in blue and cyan KAL with and without estimating the celestial pole offsets using the GPS noise, and in magenta KAL_{LSM} estimated using the LSM noise. In black the 3σ (solid) and 1σ (dashed) confidence level.

Not only leads the LSM noise to an significant increase of the power at higher frequencies, but also additional significant peaks arise at integer hours, easily discernible at ±8 h, ±7 h and ±6 h. More importantly, the filter is no longer able to de-correlate retrograde polar motion and nutation, as nutation is highly underestimated. Hence, where for KAL (blue) the peak at −24 h reaches the 1σ confidence level of LSM, for KAL_{GPS} it surpasses even KAL where no nutation was estimated (cyan) and almost reaches LSM (green). Increasing the noise level for celestial pole offsets of 0.01 mas^2/d by a factor of ten can not inhibit that. This confirms that the noise levels of the individual parameters cannot be chosen arbitrarily as long as they are proportional, but that they need to reflect the true physical behavior of the signal. Only this will allow a precise estimation and also de-correlation of the parameters of interest.

5. Conclusions and outlook

In this study we demonstrated the potential of the determination of EOP by Kalman filtering of VLBI data. We determined EOP from all CONT campaigns since 2002 using the Kalman filter and compared them to the EOP determined by the commonly used least squares method. We found that the Kalman filter delivers a much smoother time series while providing the highest temporal resolution. We also found that the agreement with respect to GPS can be improved by up to 50% for CONT14 using KAL.

The precision of the Kalman VLBI solution is on a level comparable to our GPS solution, whereas the least squares solution performs on average 45% worse. Especially at higher frequencies, the Kalman filter approach clearly outmatches the least squares approach. The application of the Kalman filter opens up new possibilities for high-frequency EOP studies and enables the detection of the deficiencies in the models involved in the analysis. The offsets between the techniques still needs to be explained, especially when thinking about combining EOP time series from different techniques, a path we definitely need to pursue.

The final scope of the Kalman filter approach within VLBI is the examination of high-frequency EOP and their geophysical interpretation. This includes the fine-tuning of the filter noise, and an intensive examination of all the signals involved. As diurnal and semi-diurnal tidal motions are predominately caused by the ocean tides, we will put our focus there. Of course we will also try to distinct the tides at higher frequencies. For this we will expand our data set considerably.

Acknowledgements

This work was supported by the Austrian Science Fund (FWF), project P24187-N21.

References

[1] H. Schuh, D. Behrend, VLBI: a fascinating technique for geodesy and astrometry, J. Geodyn. 61 (2012) 68–80, http://dx.doi.org/10.1016/j.jog.2012.07.007.

[2] H. Schuh, J. Böhm, Very long baseline interferometry for geodesy and astrometry, in: G. Xu (Ed.), Sciences of Geodesy II: Innovations and Future Developments, Springer, 2013.
[3] Z. Altamimi, X. Collilieux, L. Métivier, ITRF2008: an improved solution of the international terrestrial reference frame, J. Geod. 85 (8) (2011) 457–473.
[4] A.L. Fey, D. Gordon, C.S. Jacobs, C. Ma, R.A. Gaume, E.F. Arias, G. Bianco, D.A. Boboltz, S. Bckmann, S. Bolotin, P. Charlot, A. Collioud, G. Engelhardt, J. Gipson, A.M. Gontier, R. Heinkelmann, S. Kurdubov, S. Lambert, S. Lytvyn, D.S. MacMillan, Z. Malkin, A. Nothnagel, R. Ojha, E. Skurikhina, J. Sokolova, J. Souchay, O.J. Sovers, V. Tesmer, O. Titov, G. Wang, V. Zharov, The second realization of the iternational celestial reference frame by very long baseline interferometry, Astron. J. 150 (2) (2015).
[5] J. Dow, R.E. Neilan, C. Rizos, The international GNSS Service in a changing landscape of global navigation satellite systems, J. Geod. 83 (34) (2009) 191198.
[6] R. Heinkelmann, J. Böhm, S. Bolotin, G. Engelhardt, R. Haas, R. Lanotte, D.S. MacMillan, M. Negusini, E. Skurikhina, O. Titov, H. Schuh, VLBI-derived troposphere parameters during CONT08, J. Geod. 85 (2011), http://dx.doi.org/10.1007/s00190-011-0459-x.
[7] D. Dettmering, R. Heinkelmann, M. Schmidt, Systematic differences between VTEC obtained by different space-geodetic techniques during CONT08, J. Geod. 85 (2011) 443–451, http://dx.doi.org/10.1007/s00190-008-0300-3.
[8] C. Rieck, R. Haas, K. Jaldehag, J. Johansson, VLBI and GPS-based time-transfer using CONT08 data, in: D. Behrend, K.D. Baver (Eds.), Proceedings of IVS 2010 General Meeting: 'VLBI2010: From Vision to Reality', 2010, pp. 365–369. NASA/CP-2010–215864.
[9] T. Artz, S. Böckmann, A. Nothnagel, P. Steigenberger, Sub-diurnal variations in the Earth's rotation from continuous VLBI campaigns, J. Geophys. Res. 115 (B05) (2010) 404, http://dx.doi.org/10.1029/2009JB006834.
[10] R. Haas, J. Wünsch, Sub-diurnal earth rotation variations from the VLBI CONT02 campaign, J. Geodyn. 41 (1–3) (2006) 94–99, http://dx.doi.org/10.1016/j.jog.2005.08.025.
[11] J. Nastula, B. Kolaczek, R. Weber, H. Schuh, J. Böhm, Spectra of rapid oscillations of Earth rotation parameters determined during the CONT02 campaign, in: P. Tregoning, C. Rizos (Eds.), Dynamic Planet, IAG Symposium, vol. 130, Springer, Heidelberg, 2007, pp. 208–214.
[12] T. Nilsson, J. Böhm, M. Schindelegger, H. Schuh, High frequency Earth rotation parameters estimated from the CONT campaigns, in: D. Behrend, K.D. Baver (Eds.), Proceedings of IVS 2012 General Meeting: Launching the Next-Generation IVS Network, NASA/CP-2012-217504, 2012, pp. 390–394. http://ivscc.gsfc.nasa.gov/publications/gm2012/nilsson.pdf.
[13] T. Nilsson, J. Böhm, H. Schuh, Sub-diurnal Earth rotation variations observed by VLBI, Artif. Satell. 42 (2) (2010) 49–55, http://dx.doi.org/10.2478/v10018-010-0005-8.
[14] T. Nilsson, R. Heinkelmann, M. Karbon, V. Raposo-Pulido, B. Soja, H. Schuh, Earth orientation parameters estimated from VLBI during the CONT11 campaign, J. Geod. 88 (2014) 491–502, http://dx.doi.org/10.1007/s001902-014-0700-5.
[15] G. Petit, B. Luzum (Eds.), IERS Conventions 2010, Verlag des Bundesamtes für Kartographie und Geodäsie, Frankfurt am Main, Germany, 2010.
[16] B. Petrachenko, A. Niell, D. Behrend, B. Corey, J. Böhm, P. Charlot, A. Collioud, J. Gipson, R. Haas, T. Hobiger, Y. Koyama, D. MacMillan, Z. Malkin, T. Nilsson, A. Pany, G. Tuccari, A. Whitney, J. Wresnik, Design aspects of the VLBI2010 system, in: D. Behrend, K. Baver (Eds.), International VLBI Service for Geodesy and Astrometry 2008 Annual Report, NASA Technical Publications, 2009. NASA/TP-2009–214183.
[17] Z. Deng, T. Schöne, G. Gendt, Status of the TIGA tide gauge data reprocessing at GFZ, Int. Assoc. Geod. Symp. (October 2013) 2014.
[18] A.T. Deller, S.J. Tingay, W. Brisken, Precision Southern Hemisphere pulsar VLBI astrometry: techniques and results for PSR J1559-4438, Astrophys. J. 690 (2009) 198–209, http://dx.doi.org/10.1088/0004-637X/690/1/198.
[19] Z. Malkin, On comparison of the Earth orientation parameters obtained from different VLBI networks and observing programs, J. Geod. 83 (2009) 547–556, http://dx.doi.org/10.1007/s00190-008-0265-2.
[20] A. Nothnagel, International VLBI Service for geodesy and astrometry (IVS), in: The IVS Data Input to ITRF2014, International VLBI Service for Geodesy and Astrometry, GFZ Data Services, 2015, http://dx.doi.org/10.5880/GFZ.1.1.2015.002.
[21] J. Böhm, S. Böhm, T. Nilsson, A. Pany, L. Plank, H. Spicakova, K. Teke, H. Schuh, The new Vienna VLBI software, in: S. Kenyon, M.C. Pacino, U. Marti (Eds.), IAG Scientific Assembly 2009, 2012, p. 136.
[22] T. Nilsson, B. Soja, M. Karbon, R. Heinkelmann, H. Schuh, Application of Kalman filtering in VLBI data analysis, Earth Planets Space 67 (2015) 136.
[23] J. Böhm, B. Werl, H. Schuh, Troposphere mapping functions for GPS and very long baseline interferometry from European centre for medium-range weather forecasts operational analysis data, J. Geophys. Res. 111 (B02) (2006) 406, http://dx.doi.org/10.1029/2005JB003629.
[24] S. Böckmann, T. Artz, A. Nothnagel, VLBI terrestrial reference frame contributions to ITRF2008, J. Geod. 84 (2010) 201–219, http://dx.doi.org/10.1007/s00190-009-0357-7.
[25] T. Artz, S. Böckmann, A. Nothnagel, V. Tesmer, EOP time series with daily and sub-daily resolution determined from CONT05, in: J. Böhm, A. Pany, H. Schuh (Eds.), Proceedings of the 18th Working Meeting European VLBI for Geodesy and Astrometry, Vienna, Austria, 2007, pp. 69–74.
[26] R.E. Kalman, A new approach to linear filtering and prediction problems, J. Basic. Eng. 82D (1960) 35–45.
[27] A. Gelb, J.F. Kasper, R.A. Nash, C.F. Prince, A.A. Sutherland, Applied Optimal Estimation, The M.I.T Press, 1974.
[28] D.W. Allan, Statistics of atomic frequency standards, Proc. IEEE (1966) 221–230.
[29] B. Soja, T. Nilsson, M. Karbon, F. Zus, G. Dick, Z. Deng, J. Wickert, R. Heinkelmann, H. Schuh, Tropospheric delay determination by Kalman filtering VLBI data, Earth Planets Space 67 (1) (2015) 1–16, http://dx.doi.org/10.1186/s40623-015-0293-0.
[30] T.A. Herring, J.L. Davis, I.I. Shapiro, Geodesy by radio interferometry: the application of Kalman filtering to the analysis of Very Long Baseline Interferometry data, J. Geophys. Res. 95 (B8) (1990) 12561–12581.
[31] D.D. McCarthy, B. Luzum, Prediction of Earth orientation, Bull. Géod. 65 (1991) 18–21.
[32] J. Ray, presentation, presented 13.05.2013, Wuhan, China, in: GNSS Observations of Earth Orientation 1, 2013, http://www.ngs.noaa.gov/web/science_edu/presentations_library/files/science_edu/presentations_library/files/whu13-gnss-erps-1.ppt.
[33] D.D. Morabito, T.M. Eubanks, J.A. Steppe, Kalman filtering of earth orientation changes, in: A. Babcock, G.A. Wilkins (Eds.), The Earths Rotation and Reference Frames for Geodesy and Geodynamics, 257–267, Dordrecht, Holland, 1988.
[34] S.D.P. Williams, Y. Bock, P. Fang, P. Jamason, R.M. Nikolaidis, L. Prawirodirdjo, M. Miller, D.J. Johnson, Error analysis of continuous GPS position time series, J. Geophys. Res. Solid Earth 109 (B3) (2004), http://dx.doi.org/10.1029/2003JB002741.
[35] T. Schöne, N. Schön, D. Thaller, IGS tide gauge Benchmark monitoring pilot project (TIGA): scientific benefits, J. Geod. 83 (2009) 249/261, http://dx.doi.org/10.1007/s00190-008-0269-y.
[36] N. Capitaine, P.M. Mathews, V. Dehant, P.T. Wallace, S.B. Lambert, On the IAU 2000/2006 precessionnutation and comparison with other models and VLBI observations, Celest. Mech. Dyn. Astron. 103 (2) (2009) 179–190, http://dx.doi.org/10.1007/s10569-008-9179-9.
[37] P. Rebischung, J. Griffiths, J. Ray, R. Schmid, X. Collilieux, B. Garayt, IGS08: the IGS realization of ITRF2008, GPS Solut. 16 (4) (2011) 483–494, http://dx.doi.org/10.1007/s10291-011-0248-2.
[38] S.D. Desai, A.E. Sibois, Evaluating predicted diurnal and semidiurnal tidal variations in polar motion with GPS-based observations, J. Geophys. Res. Solid Earth 121 (7) (2016) 5237–5256, http://dx.doi.org/10.1002/2016JB013125.
[39] P. Steigenberger, Reprocessing of a Global GPS Network, DGK, Verlag der Bayerischen Akademie der Wissenschaften, 2009, p. C:640.
[40] A. Brzeziński, C. Bizouard, S.D. Petrov, Influence of the atmosphere on Earth rotation: what new can be learned from the recent atmospheric angular momentum estimates? Surv. Geophys. 23 (1) (2002) 33–69, http://dx.doi.org/10.1023/A:1014847319391.
[41] M. Schindelegger, D. Einspigel, D. Salstein, J. Böhm, The global S_1 Tide in Earth's Nutation, Surv. Geophys. 37 (3) (2016) 643–680, http://dx.doi.org/10.1007/s10712-016-9365-3.
[42] M.G. Rochester, O.G. Jensen, D.E. Smylie, A search for the Earth's "nearly diurnal free wobble", Geophys. J. R. Astron. Soc. 38 (2) (1974) 349–363, http://dx.doi.org/10.1111/j.1365-246X.1974.tb04127.x.
[43] O. de Viron, G. Schwarzbaum, F. Lott, V. Dehant, Diurnal and subdiurnal effects of the atmosphere on the Earth rotation and geocenter motion, J. Geophys. Res. 110 (2005) B11404, http://dx.doi.org/10.1029/2005JB003761.
[44] M. Schindelegger, J. Böhm, D. Salstein, H. Schuh, High-resolution atmospheric angular momentum functions related to Earth rotation parameters during CONT08, J. Geod. 85 (7) (2011) 425–433, http://dx.doi.org/10.1007/s00190-011-0458-y.
[45] A. Brzeziński, R.M. Ponte, A.H. Ali, Nontidal oceanic excitation of nutation and diurnal/semidiurnal polar motion revisited, J Geophys. Res. 109 (2004) B11407, http://dx.doi.org/10.1029/2004JB003054.
[46] A. Brzeziński, On the influence of diurnal atmospheric tides on Earth rotation, in: N. Capitaine (Ed.), Journes Systmes de Référence Spatio Temporels 2007, 2008, pp. 180–183.

[47] E. Brockmann, Combination of solutions for geodetic and geophysical applications of the global positioning system (GPS) (Ph.D. thesis), Geod. Geophys. Arb. Schweiz 55 (1997).
[48] D. Thaller, M. Krügel, M. Rothacher, V. Tesmer, R. Schmid, D. Angermann, Combined Earth orientation parameters based on homogeneous and continuous VLBI and GPS data, J. Geod. 81 (6–8) (2007) 529–541, http://dx.doi.org/10.1007/s00190-006-0115-z.

Maria Karbon obtained her Diploma in Geodesy & Geophysics from the Technische Universität Wien in 2009, where she also worked as a project assistant until the end of 2012 and obtained her PhD. Since 2013, she works as a postdoctoral researcher at the German Research Centre for Geosciences, Potsdam.